Solvent-free autocatalytic supramolecular polymerization

Zhen Chen,[1,2] Yukinaga Suzuki,[1,2] Ayumi Imayoshi,[1] Xiaofan Ji,[1] Kotagiri Venkata Rao,[1] Yuki Omata,[1] Daigo Miyajima,[1]* Emiko Sato,[1] Atsuko Nihonyanagi[1] and Takuzo Aida[1,2]*

[1] RIKEN Center for Emergent Matter Science, 2-1 Hirosawa, Wako, Saitama 351-0198, Japan.

[2] Department of Chemistry and Biotechnology, School of Engineering, The University of Tokyo, 7-3-1 Hongo, Bunkyo-ku, Tokyo 113-8656, Japan.

* To whom correspondence should be addressed.

E-mail: aida@macro.t.u-tokyo.ac.jp (T.A.), daigo.miyajima@riken.jp (D.M.)

Research Square

Preprints are preliminary reports that have not undergone peer review. They should not be considered conclusive, used to inform clinical practice, or referenced by the media as validated information.

Abstract: Solvent-free chemical manufacturing is one of the awaited technologies for addressing an emergent issue of serious environmental pollution. Here, we report "solvent-free autocatalytic supramolecular polymerization (SF-ASP)", where a phthalonitrile derivative with hydrogen-bonding side chains as the monomer is autocatalytically transformed into the corresponding phthalocyanine in an exceptionally high yield (> 80%). The target phthalocyanine, if any is produced, nucleates and initiates supramolecular polymerization via a hydrogen-bonding interaction, affording one-dimensional single-crystalline fibers. These crystalline fibers possibly preorganize the precursor phthalonitrile monomer at their cross-sectional edges and autocatalytically convert them into the phthalocyanine under out-of-equilibrium conditions. In the presence of metal oleates, SF-ASP autocatalytically affords single-crystalline fibers of metallophthalocyanines again in exceptionally high yields. In these cases, such fibers grow in both directions without terminal coupling until the precursor phthalonitrile is completely consumed. By taking advantage of this quasi-living character of polymerization, multistep SF-ASP without/with metal oleates affords multi-block supramolecular copolymers.

Considering an emergent environmental issue caused by plastic waste[1], supramolecular polymers are the promising candidate for next-generation materials because their intrinsically dynamic nature possibly allows for excellent recyclability and recombinant usage[2,3]. Historically, supramolecular polymerization has been extensively studied in solution, and its mechanistic interpretation has been greatly elaborated in the last decade[4,5]. Nevertheless, from a viewpoint of practical applications, supramolecular polymerization under solvent-free conditions is considered more advantageous, because produced superstructures can be directly utilized as they are without losing their structural integrity. Needless to say, this process is also preferred for realizing a sustainable society[6,7]. It should be noted that, in early days of research on supramolecular polymerization, noncovalent polymeric structures were reported to form from hydrogen-bonding (H-bonding) molecules in their crystalline and liquid crystalline assemblies[8–10]. However, because of a potential difficulty in controlling such an out-of-equilibrium molecular assembly, a major interest on supramolecular polymerization moved to its solution process[11–13]. Here, we report solvent-free "autocatalytic" supramolecular polymerization (SF-ASP). Together with solvent-free chemical manufacturing, the concept of autocatalysis, which is inspired by nature, is an awaited green technology because of its potentially high selectivity and efficiency.

A chemical reaction can be called "autocatalytic" if a product of the reaction serves to catalyze its own formation. Autocatalytic chemical reactions usually show a sigmoidal time-course profile for the change in product concentration because the product facilitates its own formation[14]. Autocatalysis has been implicated in the emergence of life[15,16] and is intrinsic to many biological processes, such as the self-replication of biomolecules[17–19]. As a general strategy of autocatalytic chemical transformation, the product is designed to serve as a template (T) that can reversibly preorganize reactants A and B in the form of a ternary complex [A•T•B], which facilitates the reaction between A and B to produce T•T (ref. 20,21). However, if T•T is thermodynamically stable and does not dissociate into monomeric T, the expected autocatalytic behavior would not emerge because the concentration of active T,

which can provide ternary complex [A•T•B], drops. In 2010, Otto and coworkers reported a seminal work that, in the reversible oxidative cyclization of a dithiol having a β-sheet-forming peptide spacer, macrocyclic products with certain ring sizes, such as cyclic hexamers and heptamers, selectively form with a typical sigmoidal time-course profile if a shear force is continuously applied to the reaction mixture[22]. Why does the shear force have to be applied? In this case, the selectively formed macrocycles tend to stack into nanofibers in the reaction medium so that the concentrations of their active forms usable as the template decrease unless a shear force is continuously applied to the reaction mixture to break up the nanofibers into short pieces[23]. This work was successfully extended to the selective synthesis of other peptide amphiphiles[24–26] and demonstrates the great potential of template-assisted autocatalysis. Nevertheless, because the oxidative cyclization employed here is intrinsically reversible, the authors have not excluded that the observed product selectivity is partly due to the removal of preferred products as nanofibers from the thermodynamically equilibrated system[22].

Autocatalysis generally requires high dilution to avoid the assembly of products that act as templates. This creates a high barrier for its practical application to the large-scale manufacturing of chemicals. In contrast, self-replication events in living organisms usually operate far from thermodynamic equilibrium, and along this line, artificial out-of-equilibrium systems using chemical fuels[27], chemical oscillations[28], kinetic trapping[29,30], and microfluidic diffusion[31] as driving forces have recently been investigated. The solvent-free autocatalytic supramolecular polymerization (SF-ASP; Fig. 1a) described in the present work enables autocatalytic production of certain organic chemicals in much higher selectivity and yield than those obtained in ordinary solution processes. The monomers employed here are phthalonitrile (PN) derivatives (Fig. 1b) that adopt a fan shape with H-bonding amide groups in their side chains and serve as reactive precursors for the synthesis of phthalocyanines (^{H}PCs; Fig. 1c, left) via reductive cyclotetramerization. In SF-ASP, target ^{H}PC, if any is formed, nucleates and initiates H-bonding-mediated supramolecular polymerization to give

one-dimensional (1D) single-crystalline fibers, which possibly preorganize PN molecules via H-bonding at the cross-sectional fiber edges and efficiently template reductive cyclization to give ^{H}PC in an autocatalytic manner (Fig. 1a). When SF-ASP is conducted in the presence of metal oleates, metal complexes of phthalocyanines (^{M}PCs; Fig. 1c, right) solely form in an autocatalytic manner without contamination of their free bases.

We serendipitously found the basic principle of SF-ASP during a study on the ferroelectric nature of H-bonding PN derivatives[32], where green-colored thin fibers formed upon heating PN_{C4} (Fig. 1b) on a hot stage. As described in Methods, when a powdery sample of PN_{C4}, sandwiched with glass plates, was heated to a hot melt and kept at 160 °C for 15 hours, numerous green-colored thin fibers formed (Fig. 2d, right). The fibers began to appear approximately 4 hours after heating and then developed entirely and elongated abruptly (Fig. 2d, Supplementary Video 1). By matrix-assisted laser desorption ionization time-of-flight (MALDI-TOF) mass spectrometry (Fig. 2c, i), we found that the fibers obtained in 24 hours were composed of phthalocyanine $^{H}PC_{C4}$ (Fig. 1c), whereas no precursor PN_{C4} was detected. This crude product, when simply washed with methanol, gave analytically pure $^{H}PC_{C4}$ (Supplementary Fig. 1). A change in the absorption intensity at 700 nm assignable to $^{H}PC_{C4}$ (Supplementary Fig. 1d) clearly showed a sigmoidal time-course profile (Fig. 2a, black). Further systematic studies revealed that SF-ASP of PN_{C4} can be considerably affected by the reaction temperature (Supplementary Figs. 2–4). As shown in Fig. 2b and Supplementary Table 1, when SF-ASP was carried out by elevating the temperature from 160 °C to 190 °C, the yield of $^{H}PC_{C4}$ after 24 hours was considerably enhanced from 53% to 83%. This value is far better than those reported for the ordinary solution synthesis of ^{H}PC derivatives (20–25%; see Supplementary Methods). However, when the temperature was elevated further, the yield of $^{H}PC_{C4}$ started to drop due to the formation of a considerable amount of side products.

We likewise heated PN_{C5} and PN_{C6} containing longer hydrocarbon chains than PN_{C4} (Fig. 1b) but did not observe any autocatalytic feature (Fig. 2a, green and blue, respectively). For example, the reaction mixture of PN_{C6} upon heating at 160 °C was entirely green with no fibrous assembly (Fig. 2e, ii). MALDI-TOF mass spectrometry of the reaction mixture (Fig. 2c, ii) showed poor selectivity for $^{H}PC_{C6}$ (Fig. 1c, Supplementary Table 2). Although heating PN_{C5} at 160 °C resulted in the formation of short green fibers (Fig. 2e, i), their structural integrity appeared to be much lower than the case of using PN_{C4} for SF-ASP (Fig. 2d). When *N*-methylated $PN_{C4}^{N\text{-Me}}$ without H-bonding capability (Fig. 1b) was heated at 160 °C, no fibrous assembly appeared (Fig. 2e, iii), and accordingly, no autocatalytic feature emerged (Fig. 2a, red), affording $^{H}PC_{C4}^{N\text{-Me}}$ (Fig. 1c) with very poor selectivity (Fig. 2c, iii, Supplementary Table 2).

A study using polarizing optical microscopy (Fig. 3a) revealed that the as-formed $^{H}PC_{C4}$ fibers obtained by SF-ASP were highly crystalline. Powder X-ray diffraction (PXRD) analysis (Fig. 3b) of the crystalline fibers of as-formed $^{H}PC_{C4}$, denoted hereafter as $[^{H}PC_{C4}]^{CF}$ (CF: crystalline fiber) displayed intense diffraction peaks that were indexed to those for a hexagonally packed columnar assembly (Fig. 3b, inset). Notably, through-view two-dimensional (2D) small-angle X-ray scattering (SAXS) analysis of a single fiber of $[^{H}PC_{C4}]^{CF}$ (Fig. 3c) revealed a single-crystal-like pattern, where spot-type reflections assignable to the (100), (110), and (300) planes of the hexagonal geometry appeared only in the direction perpendicular to the *c* axis of the crystalline lattice. This result demonstrates that the crystalline lattice of $[^{H}PC_{C4}]^{CF}$ aligns along the longer axis of the fiber (Fig. 3b, inset). Its selected-area electron diffraction (SAED) pattern (Fig. 3d) displayed two symmetric spots that were indexed to the (001) plane in the direction along the longer axis of the fibers, suggesting that each column comprised a cofacial π-stack of $^{H}PC_{C4}$ (Fig. 3f). Likewise, in the polarized Fourier transform infrared (FT-IR) spectra of $[^{H}PC_{C4}]^{CF}$ (Fig. 3e), the stretching vibrations due to the N–H (3282 cm^{-1}) and C=O (1620 cm^{-1}) groups both showed their maximum absorbance in the direction parallel (θ = 0°) to the longer axis of the fiber.

Consistent with the SAXS (Fig. 3c) and SAED (Fig. 3d) patterns described above, this dichroic feature indicates that the H-bonded amide groups align unidirectionally along the supramolecular polymer chain (Fig. 3f).

We chromatographically isolated $^{H}PC_{C5}$, $^{H}PC_{C6}$, and $^{H}PC_{C4}{}^{N\text{-Me}}$ from the reaction mixtures and found that, upon being slowly cooled from their isotropic hot melts, $^{H}PC_{C5}$ and $^{H}PC_{C6}$ except $^{H}PC_{C4}{}^{N\text{-Me}}$ self-assembled into hexagonally packed 1D crystalline fibers $[^{H}PC_{C5}]^{CF}$ and $[^{H}PC_{C6}]^{CF}$ (Supplementary Fig. 5). Their intercolumnar distances were 3.89 nm and 4.12 nm, respectively, which are larger than that of $[^{H}PC_{C4}]^{CF}$ (3.66 nm) as expected from their molecular models. Although $[^{H}PC_{C5}]^{CF}$ and $[^{H}PC_{C6}]^{CF}$ are thus geometrically identical to $[^{H}PC_{C4}]^{CF}$, there exists a certain difference in their thermal stabilities, which surely affect the features of SF-ASP. The differential scanning calorimetry (DSC) profiles (Fig. 2f, Supplementary Fig. 6) indicate that only $[^{H}PC_{C4}]^{CF}$ (T_m = 204 °C) can survive without melting at 160–200 °C, which is the optimum temperature range for the chemical transformation of PN_{C4} to $^{H}PC_{C4}$ occur (Fig. 2b, Supplementary Fig. 2), whereas $[^{H}PC_{C5}]^{CF}$ (T_m = 158 °C) and $[^{H}PC_{C6}]^{CF}$ (T_m = 141 °C) melt when heated at 160 °C. Namely, for SF-ASP to work, the products must be assembled into single-crystalline fibers even at high temperatures. Heating PN_{C4} in the bulk state at 160 °C, for example, resulted in the formation of $^{H}PC_{C4}$, which assembled into $[^{H}PC_{C4}]^{CF}$ with a clear induction period of 3–4 hours (Figs. 2a, black and 2d). As illustrated in Fig. 1a, the cross-sectional fiber edges may certainly preorganize the PN_{C4} molecules via H-bonding interactions, thereby allowing them to reductively cyclotetramerize into $^{H}PC_{C4}$ efficiently. Then, a new set of the PN_{C4} molecules can likewise be preorganized on the newly formed cross-sectional fiber edges. Repetition of the sequence of these elementary steps should result in elongation of $[^{H}PC_{C4}]^{CF}$. As shown in Supplementary Video 1, the green fibers of $[^{H}PC_{C4}]^{CF}$ started to form 3–4 hours after heating and then continuously elongated and increased in their number and thickness over a period of an additional 4 hours (Supplementary Fig. 7). In a subsequent stage, although new fiber formation subsided, the preformed fibers still became thicker. Fiber

thickening, leading to an increase in the cross-sectional area of the fibers, promotes the autocatalytic conversion of PN_{C4} into $^{H}PC_{C4}$, so that PN_{C4} is completely consumed. Equally important, fiber elongation by chain coupling, leading to a decrease in the cross-sectional area of the fibers, barely occurs in SF-ASP, certainly due to the very sluggish diffusion of bundled polymer chains under solvent-free conditions. Therefore, we conclude that SF-ASP has a great advantage over reported autocatalytic processes in solution, where chain coupling to lower the autocatalytic activity is inevitable[22–26].

Although the mechanism has yet to be clarified[33], the cyclotetramerization of PN_{C4} into $^{H}PC_{C4}$ is a H^+-mediated reductive process: $4PN_{C4} + 2H^+ + 2e^- \rightarrow {}^{H}PC_{C4}$. Therefore, the solution synthesis of ^{H}PCs is often conducted in protic solvents, such as alcohols. For SF-ASP, we consider that surface silanol groups on the glass substrate may play a similar role as alcohols. Although the number of surface silanol groups is limited, a siloxane bridge (≡Si−O−Si≡) upon heating over 160 °C was reported to cleave off homolytically to produce radical species ≡Si• and •O−Si≡, which in turn react with a water molecule to generate H^+ and e^- (ref. 34,35). The above process is considered essential for the H^+-mediated reductive cyclotetramerization of PN precursors. Accordingly, when PN_{C4} was freeze-dried and employed for SF-ASP in a dry N_2 atmosphere, the yield of $^{H}PC_{C4}$ dropped significantly from 81% to 32% (Supplementary Fig. 8).

SF-ASP also works for the selective synthesis of metallophthalocyanines, which have the higher potential for practical applications than free-base phthalocyanines[36–38]. Examples in the present work include zinc (Zn), iron (Fe), cobalt (Co), and copper (Cu) phthalocyanines ($^{M}PC_{C4}$; Fig. 1c), which were selectively produced in high yields (77–90%; Supplementary Table 2) simply by heating PN_{C4} in the presence of metal oleate salts (see Methods). Typically, a 2:1 molar mixture of PN_{C4} and $Zn(oleate)_2$, sandwiched with glass plates, was heated at 160 °C for 12 hours, whereupon a change in its absorption intensity at 700 nm due to $^{Zn}PC_{C4}$ (Supplementary Fig. 9a) clearly displayed a sigmoidal time-course profile (Fig. 4a,

blue) with a shorter induction period than that without Zn(oleate)$_2$ (Fig. 2a, black). We also found that, after the induction period, green-colored single-crystalline fibers developed entirely (Fig. 4b, i). By elemental mapping using scanning electron microscopy/energy dispersive X-ray spectroscopy (SEM-EDX; Supplementary Fig. 9b) together with MALDI-TOF mass spectrometry (Supplementary Fig. 9c), we confirmed that the as-formed fibers are composed solely of ^{Zn}PC$_{C4}$ without any trace of free-base ^{H}PC$_{C4}$. The same held true for the SF-ASP of PN$_{C4}$ with other oleate salts of Fe (Figs. 4a, orange and 4b, ii, Supplementary Fig. 10), Co (Figs. 4a, purple and 4b, iii, Supplementary Fig. 11), and Cu (Figs. 4a, red and 4b, iv, Supplementary Fig. 12). Heating free-base ^{H}PC$_{C4}$ with the above metal oleates for 24 hours resulted in only poor yields of ^{M}PC$_{C4}$ (Supplementary Fig. 13), suggesting that the metal ion is involved in the transition state of the autocatalytic process of SF-ASP.

Although the SF-ASP of PN$_{C4}$ to form [^{H}PC$_{C4}$]^{CF} or [^{M}PC$_{C4}$]^{CF} should, in principle, follow the step-growth mechanism, due to the sluggish diffusion kinetics under solvent-free conditions, chain coupling is prevented (Supplementary Video 1 and Fig. 7), so that the single-crystalline fibers grow continuously in both directions until PN$_{C4}$ is completely consumed, similar to living chain-growth processes[39–41]. Hence, we envisioned that one could synthesize block copolymers by multistep SF-ASP using PN$_{C4}$ in combination with different metal oleates (see Methods). As a typical example, active seeds of [^{Cu}PC$_{C4}$]^{CF} were prepared by chopping its as-formed fibers for 10 seconds in methanol, and the resulting suspension was cast onto a glass plate and air-dried. This glass plate was covered with powdery PN$_{C4}$, and the mixture was sandwiched with glass plates and heated at 180 °C, whereupon [^{Cu}PC$_{C4}$]^{CF} in a hot melt of PN$_{C4}$ started to grow uniformly in both directions, affording the ABA-type of triblock copolymer [^{H}PC$_{C4}$]^{CF}-[^{Cu}PC$_{C4}$]^{CF}-[^{H}PC$_{C4}$]^{CF} in 4 hours (Supplementary Fig. 14d). Although its block segments were easily differentiated by their intrinsic colors (Fig. 4c, ii), elemental mapping with SEM-EDX (Supplementary Fig. 15) allowed us to confirm that copper, as expected, was localized only in its middle block

segment, whereas sulfur was distributed over the entire fiber. Meanwhile, the through-view 2D SAXS patterns collected from the $[^{Cu}PC_{C4}]^{CF}$ and $[^{H}PC_{C4}]^{CF}$ segments (Supplementary Fig. 16) revealed that their structural integrities were both very high. These observations allow us to conclude that the cross-sectional fiber edges template the epitaxial growth of the $[^{H}PC_{C4}]^{CF}$ segment, affording a 1D supramolecular heterojunction[42–44]. However, note that SF-ASP in the second stage, when conducted for more than 4 hours (Fig. 2d), concomitantly gave a nonnegligible amount of homotropic $[^{H}PC_{C4}]^{CF}$. After struggling, we eventually found that this unfavorable process was suppressed when SF-ASP was conducted using glass plates coated with an amorphous perfluoropolymer called CYTOP™ (Supplementary Fig. 17) and successfully obtained a variety of ABA- and even ABCBA-types of multi-block copolymers (Fig. 4c, Supplementary Fig. 14). Another important key to obtain well-defined multi-block copolymers was to combine block segments whose intercolumnar distances should match with less than a 2.0% difference (Fig. 4d, Supplementary Fig. 18 and Table 4). In fact, in the multistep SF-ASP of PN_{C4} and PN_{C3} (Fig. 1b), where the difference in the intercolumnar distances between $[^{H}PC_{C4}]^{CF}$ (3.66 nm) and $[^{H}PC_{C3}]^{CF}$ (3.35 nm) exceeds 9% (Fig. 4d, Supplementary Fig. 19 and Table 3), the blocked segments were highly branched (Fig. 4e).

Finally, we would like to point out that in SF-ASP, the growth direction of the single-crystalline fibers can be controlled by the type of substrate employed. For example, when PN_{C4} was heated between glass plates whose surfaces were rubbed in advance with a polytetrafluoroethylene (PTFE) rod and parallelly oriented, the resulting $[^{H}PC_{C4}]^{CF}$ fibers were preferentially oriented along the rubbed direction (Fig. 4f, i). Of particular interest, when single-crystalline potassium bromide (KBr) plates were employed to sandwich PN_{C4}, SF-ASP gave grid-like 2D crosslinked fibers of $[^{H}PC_{C4}]^{CF}$ (Fig. 4f, ii). We also found that the SF-ASP of PN_{C4}, when conducted with $Fe(oleate)_3$ in a 10-*T* magnetic field, resulted in the formation of $[^{Fe}PC_{C4}]^{CF}$ that were preferentially oriented orthogonal to the magnetic flux line (Fig. 4g, i). In contrast, the SF-ASP of PN_{C4} (Fig. 4g, iii) and $PN_{C4}/Co(oleate)_2$ (Fig. 4g,

ii) under the same conditions did not form oriented fibers. Since $[^{Fe}PC_{C4}]^{CF}$ once formed were not magnetically orientable afterwards, we consider that the magnetic field surely affected the nucleation process of SF-ASP. Computational simulations (Supplementary Fig. 20) suggested that crystalline nuclei consisting of ~10^5 molecules of $^{Fe}PC_{C4}$ likely align perpendicular to the magnetic flux line, whereas those consisting of $^{H}PC_{C4}$ and $^{Co}PC_{C4}$ align randomly.

Outlook

There exists a preconception that supramolecular polymerization under solvent-free conditions, due to its out-of-equilibrium nature, may afford a complicated mixture of different assembled structures including cyclic oligomers. Perhaps for this reason, solvent-free supramolecular polymerization has rarely been explored to date. However, as highlighted in the present paper, we eventually updated this preconception through our serendipitous finding made during a study on the thermal properties of liquid crystalline phthalonitriles. Namely, under solvent-free conditions, the supramolecular polymer can grow regularly with a quasi-living nature, affording ABA and ABCBA-types of multi-block copolymers. Even more importantly, the growing polymer preorganizes the phthalonitrile monomer molecules at its cross-sectional edges and autocatalytically converts them into the corresponding phthalocyanine and its metal complexes in exceptionally high selectivity and yield. Solvent-free autocatalytic supramolecular polymerization, thus unveiled, may certainly show one of the ideal forms of polymer manufacturing for the sustainable future.

References

1. Lau, W. W. Y. et al. Evaluating scenarios towards zero plastic pollution. *Science* **369**, 1455–1461 (2020).
2. Aida, T., Meijer, E. W. & Stupp, S. I. Functional supramolecular polymers. *Science* **335**, 813–817 (2012).
3. Aida, T. & Meijer, E. W. Supramolecular polymers–we've come full circle. *Isr. J. Chem.* **60**, 33–47 (2020).
4. De Greef, T. F. A. et al. Supramolecular polymerization. *Chem. Rev.* **109**, 5687–5754 (2009).
5. Hashim, P. K., Bergueiro, J., Meijer, E. W. & Aida, T. Supramolecular polymerization: a conceptual expansion for innovative materials. *Prog. Polym. Sci.* **105**, 101250 (2020).
6. Tanaka, K. & Toda, F. Solvent-free organic synthesis. *Chem. Rev.* **100**, 1025–1074 (2000).
7. Zimmerman, J. B., Anastas, P. T., Erythropel, H. C. & Leitner, W. Designing for a green chemistry future. *Science* **367**, 397–400 (2020).
8. Zerkowski, J. A., Seto, C. T., Wierda, D. A. & Whitesides, G. M. Design of organic structures in the solid state: Hydrogen-bonded molecular "tapes". *J. Am. Chem. Soc.* **112**, 9025–9026 (1990).
9. Fouquey, C., Lehn, J. M. & Levelut, A. M. Molecular recognition directed self-assembly of supramolecular liquid crystalline polymers from complementary chiral components. *Adv. Mater.* **2**, 254–257 (1990).
10. Lee, C. M., Jariwala, C. P. & Griffin, A. C. Heteromeric liquid-crystalline association chain polymers: Structure and properties. *Polymer* **35**, 4550–4554 (1994).
11. Rao, K. V., Miyajima, D., Nihonyanagi, A. & Aida, T. Thermally bisignate supramolecular polymerization. *Nat. Chem.* **9**, 1133–1139 (2017).
12. Van Zee, N. J. et al. Potential enthalpic energy of water in oils exploited to control supramolecular structure. *Nature* **558**, 100–103 (2018).
13. Datta, S. et al. Self-assembled polycatenanes from supramolecular toroidal building blocks *Nature* **583**, 400–405 (2020).
14. Bissette, A. J. & Fletcher, S. P. Mechanism of autocatalysis. *Angew. Chem. Int. Ed.* **52**, 12800–12826 (2013).
15. Schrodinger, E. *What Is Life—The Physical Aspect of the Living Cell* (Cambridge Univ. Press, Cambridge, 1944).

16. Robertson, M. P. & Joyce, G. F. The origins of the RNA world. *Cold Spring Harbor Perspect. Biol.* **4**, a003608 (2012).

17. Orgel, L. E. Molecular replication. *Nature* **358**, 203–209 (1992).

18. Lee, D. H., Granja, J. R., Martinez, J. A., Severin, K. & Ghadiri, M. R. A self-replicating peptide. *Nature* **382**, 525–528 (1996).

19. Paul, N. & Joyce, G. F. A self-replicating ligase ribozyme. *Proc. Natl. Acad. Sci. U.S.A.* **99**, 12733–12740 (2002).

20. Robertson, A., Sinclair, A. J. & Philp, D. Minimal self-replicating systems. *Chem. Soc. Rev.* **29**, 141–152 (2000).

21. Vidonne, A. & Philp, D. Making molecules make themselves—the chemistry of artificial replicators. *Eur. J. Org. Chem.* **2009**, 593–610 (2009).

22. Carnall, J. M. A. et al. Mechanosensitive self-replication driven by self-organization. *Science* **327**, 1502–1506 (2010).

23. Colomb-Delsuc, M., Mattia, E., Sadownik, J. W. & Otto, S. Exponential self-replication enabled through a fiber elongation/breakage mechanism. *Nat. Commun.* **6**, 7274 (2015).

24. Rubinov, B. et al. Transient fibril structures facilitating nonenzymatic self-replication. *ACS Nano* **6**, 7893–7901 (2012).

25. Brea, R. J. & Devaraj, N. K. Continual reproduction of self-assembling oligotriazole peptide nanomaterials. *Nat. Commun.* **9**, 730 (2018).

26. Fores, J. R. et al. Autonomous growth of spatially localized supramolecular hydrogel through emergence of autocatalytic ability. *Angew. Chem. Int. Ed.* **59**, 14558–14563 (2020).

27. Morrow, S. M., Colomer, I. & Fletcher, S. P. A chemically fueled self-replicator. *Nat. Commun.* **10**, 1011 (2019).

28. Semenov, S. N. et al. Autocatalytic, bistable, oscillatory networks of biologically relevant organic reactions. *Nature* **537**, 656–660 (2016).

29. Colomer, I., Morrow, S. M. & Fletcher, S. P. A transient self-assembling self-replicator. *Nat. Commun.* **9**, 2239 (2018).

30. Kumar M. et al. Amino-acid-encoded biocatalytic self-assembly enables the formation of transient conducting nanostructures. *Nat. Chem.* **10**, 696–703 (2018).

31. Epstein, I. R. & Xu, B. Reaction-diffusion processes at the nano- and microscales. *Nat. Nanotechnol.* **11**, 312–319 (2016).

32. Miyajima, D. et al. Ferroelectric columnar liquid crystal featuring confined polar groups within core-shell architecture. *Science* **336**, 209–213 (2012).

33. Kadish, K. M., Smith, K. M. & Guilard, R. *The Porphyrin Handbook: Phthalocyanine: Synthesis* (Academic Press, San Diego, 2003).

34. Narayanasamy, J. & Kubichi, J. D. Mechanism of hydroxyl radical generation from a silica surface: Molecular orbital calculations. *J. Phys. Chem. B* **109**, 21796–21807 (2005).

35. Gierada, M., Proft, F. D., Sulpizi, M. & Tielens, F. Understanding the acidic properties of the amorphous hydroxylated silica surface. *J. Phys. Chem. C* **123**, 17343–17352 (2019).

36. Inabe, T. & Tajima, H. Phthalocyanines—versatile components of molecular conductors. *Chem. Rev.* **104**, 5503–5533 (2004).

37. Sorokin, A. B. Phthalocyanine metal complexes in catalysis. *Chem. Rev.* **113**, 8152–8191 (2013).

38. Melville, O. A., Lessard, B. H. & Bender, T. P. Phthalocyanine-based organic thin-film transistors: a review of recent advances. *ACS Appl. Mater. Interfaces* **7**, 13105–13118 (2015).

39. Ogi, S., Sugiyasu, K., Manna, S., Samitsu, S. & Takeuchi, M. Living supramolecular polymerization realized through a biomimetic approach. *Nat. Chem.* **6**, 188–195 (2014).

40. Kang, J. et al. A rational strategy for the realization of chain-growth supramolecular polymerization. *Science* **347**, 646–651 (2015).

41. Wehner, M. & Würthner, F. Supramolecular polymerization through kinetic pathway control and living chain growth. *Nat. Rev. Chem.* **4**, 38–53 (2020).

42. Zhang, Y. et al. Organic single-crystalline p-n junction nanoribbons. *J. Am. Chem. Soc.* **132**, 11580–11584 (2010).

43. Zhang, W. et al. Supramolecular linear heterojunction composed of graphite-like semiconducting nanotubular segments. *Science* **334**, 340–343 (2011).

44. Jin, X. et al. Long-range exciton transport in conjugated polymer nanofibers prepared by seeded growth. *Science* **360**, 897–900 (2018).

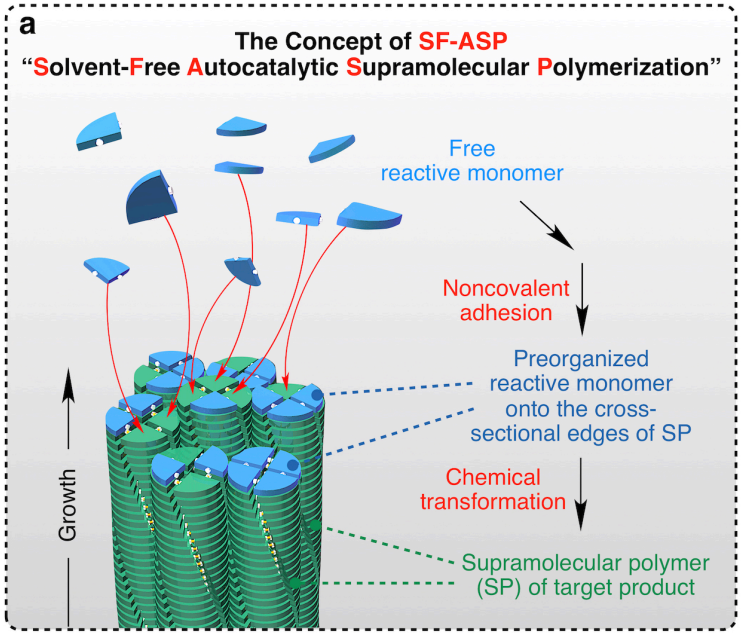
a
The Concept of SF-ASP
"Solvent-Free Autocatalytic Supramolecular Polymerization"
Free
reactive monomer
Noncovalent
adhesion
Preorganized
reactive monomer
onto the cross-
sectional edges of SP
Chemical
transformation
Supramolecular polymer
(SP) of target product
Growth

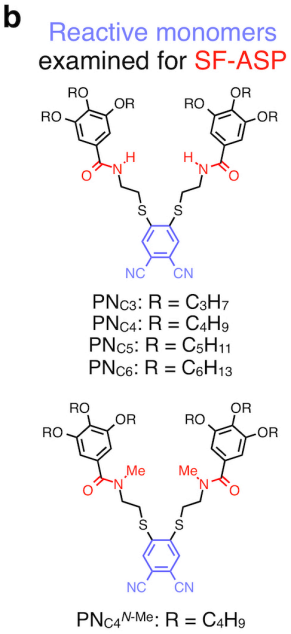
b
Reactive monomers
examined for SF-ASP
PNC3: R = C3H7
PNC4: R = C4H9
PNC5: R = C5H11
PNC6: R = C6H13
PNC4N-Me: R = C4H9

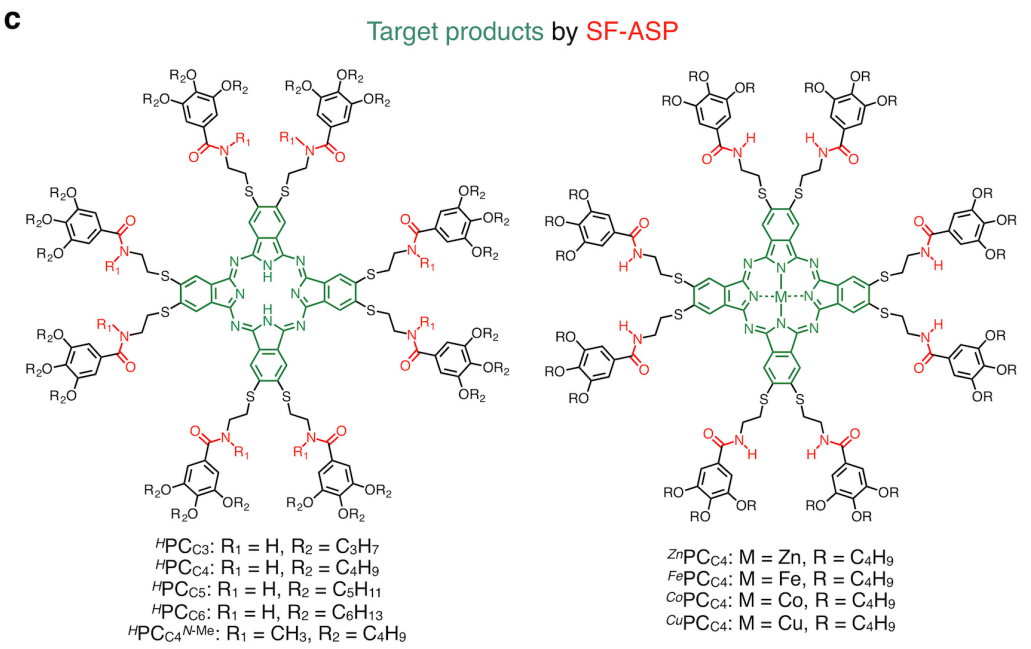
c
Target products by SF-ASP
HPC3: R1 = H, R2 = C3H7
HPC4: R1 = H, R2 = C4H9
HPC5: R1 = H, R2 = C5H11
HPC6: R1 = H, R2 = C6H13
HPC4N-Me: R1 = CH3, R2 = C4H9
ZnPC4: M = Zn, R = C4H9
FePC4: M = Fe, R = C4H9
CoPC4: M = Co, R = C4H9
CuPC4: M = Cu, R = C4H9

Fig. 1 | Autocatalysis driven by solvent-free supramolecular polymerization. **a**, Schematic illustration of the concept of solvent-free autocatalytic supramolecular polymerization (SF-ASP). The target product, if any is formed, nucleates and initiates supramolecular polymerization via a noncovalent interaction, affording 1D single-crystalline fibers. The cross-sectional fiber edges may certainly preorganize reactive monomers and efficiently promote their chemical transformation in an autocatalytic manner. Terminal coupling of fibers to attenuate the autocatalytic process is suppressed due to their sluggish diffusion under solvent-free conditions. **b**, Chemical structures of the fan-shaped dithioalkylphthalonitrile (PN) precursors used as reactive monomers for SF-ASP. **c**, Chemical structures of phthalocyanine (^{H}PC) derivatives (left) and their metal complexes (^{M}PCs) with Zn, Fe, Co, and Cu (right) obtained by the SF-ASP of PN precursors.

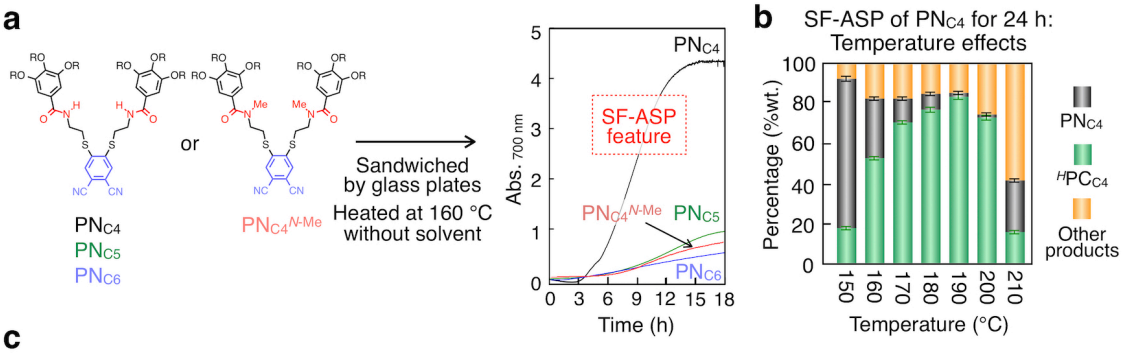

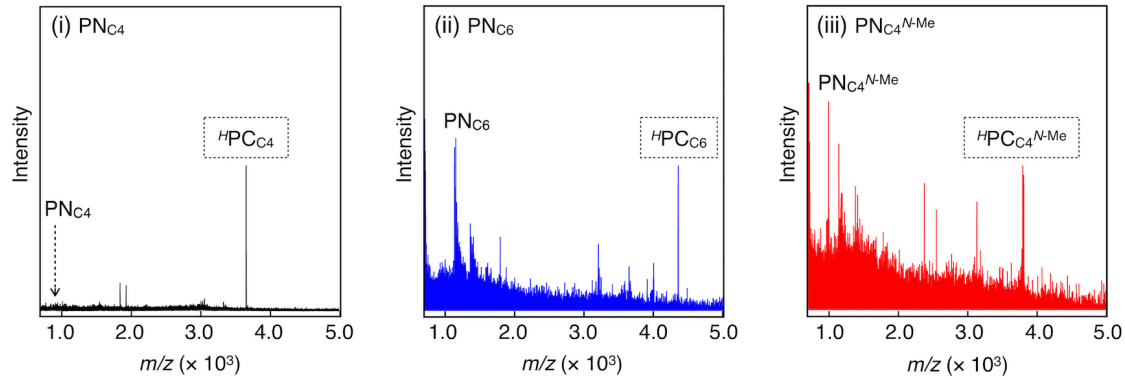

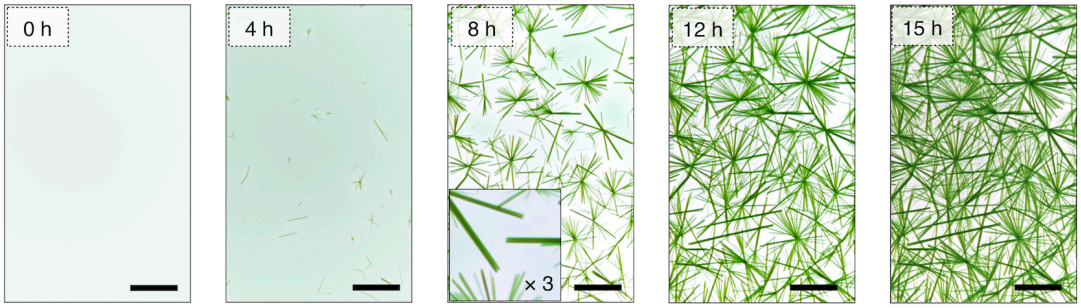

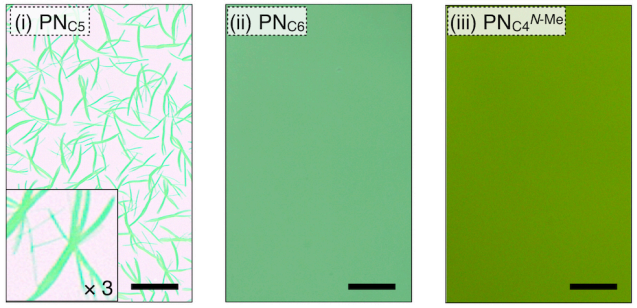

f

DSC profiles of PNs and [HPCs]CF obtained by crystallization of HPCs

PN	T_m	HPC	T_m
PN_{C4}	170 °C	HPC_{C4}	204 °C
PN_{C5}	150 °C	HPC_{C5}	158 °C
PN_{C6}	155 °C	HPC_{C6}	141 °C
$PN_{C4}^{N\text{-Me}}$	nd	$HPC_{C4}^{N\text{-Me}}$	nd

Fig. 2 | Characterization of SF-ASP. **a**, Time-dependent absorption spectral changes at 700 nm of the reaction mixtures obtained by PN_{C4} (black), PN_{C5} (green), PN_{C6} (blue), and $PN_{C4}{}^{N\text{-Me}}$ (red), sandwiched with glass plates upon heating at 160 °C, where the SF-ASP displayed a sigmoidal time-course feature. **b**, Weight fractions of $^{H}PC_{C4}$ (green bar) and PN_{C4} (black bar) as well as that of side products (orange bar) formed by the SF-ASP of PN_{C4} upon heating at different temperatures for 24 hours. **c**, MALDI-TOF mass spectra of the reaction mixtures obtained by the SF-ASP of PN_{C4} (i), PN_{C6} (ii), and $PN_{C4}{}^{N\text{-Me}}$ (iii) upon heating at 190 °C for 24 hours. **d**, Optical images of the reaction mixture obtained by the SF-ASP of PN_{C4} upon heating at 160 °C (see also Supplementary Video 1). Scale bars, 100 μm. **e**, Optical images of the reaction mixtures of SF-ASP with PN_{C5} (i), PN_{C6} (ii), and $PN_{C4}{}^{N\text{-Me}}$ (iii) after heating at 160 °C for 24 hours. Scale bars, 100 μm. **f**, DSC profiles of $[^{H}PC_{C4}]^{CF}$, $[^{H}PC_{C5}]^{CF}$, and $[^{H}PC_{C6}]^{CF}$ together with the corresponding PN derivatives. $^{H}PC_{C4}{}^{N\text{-Me}}$ did not crystallized. T_m denotes melting temperatures, while nd denotes 'not detected'.

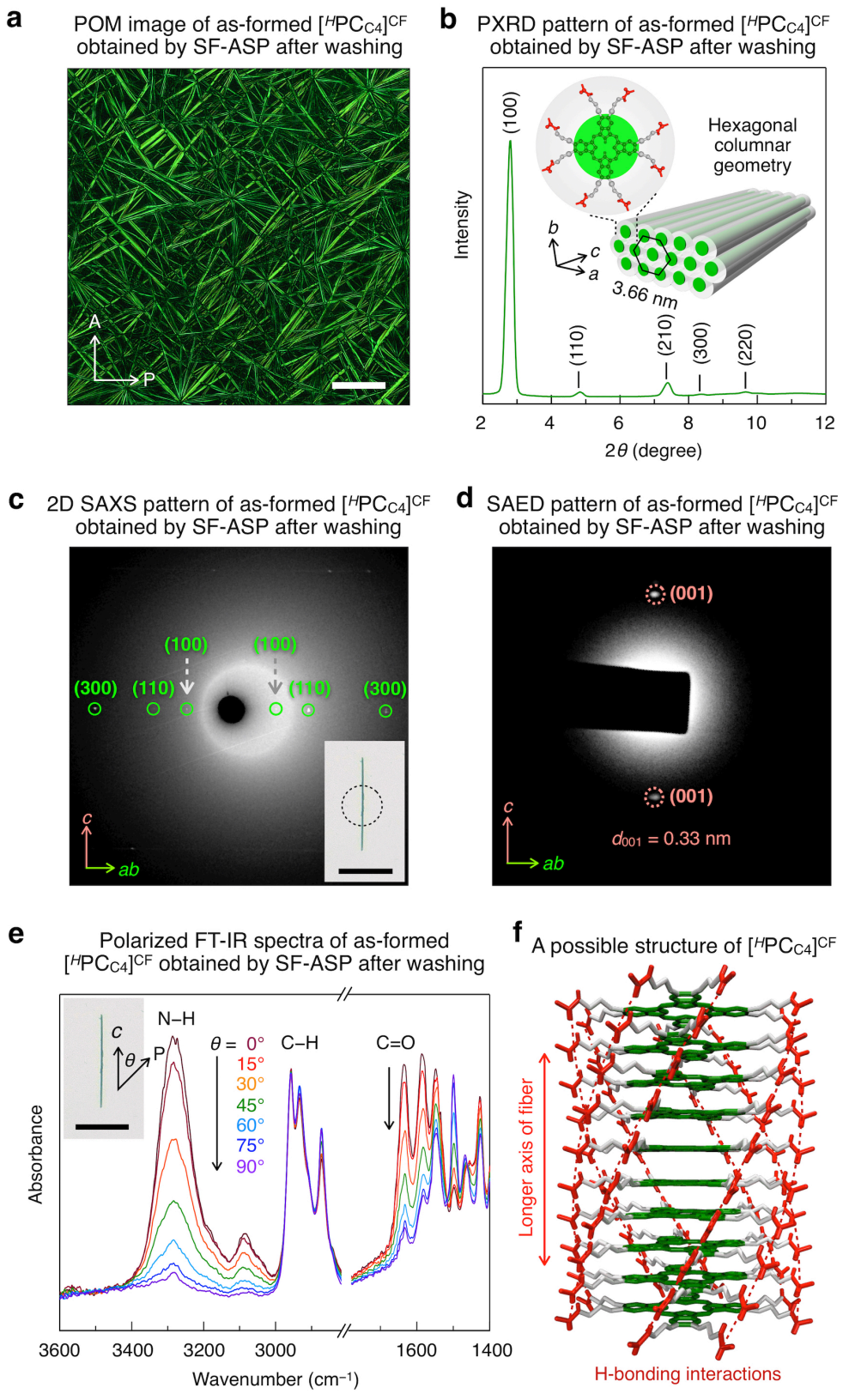
a
POM image of as-formed [HPC$_{C4}$]^{CF} obtained by SF-ASP after washing
A
P
b
PXRD pattern of as-formed [HPC$_{C4}$]^{CF} obtained by SF-ASP after washing
Hexagonal columnar geometry
3.66 nm
Intensity
(100)
(110)
(210)
(300)
(220)
2θ (degree)
c
2D SAXS pattern of as-formed [HPC$_{C4}$]^{CF} obtained by SF-ASP after washing
(100)
(100)
(300)
(110)
(110)
(300)
d
SAED pattern of as-formed [HPC$_{C4}$]^{CF} obtained by SF-ASP after washing
(001)
(001)
d_{001} = 0.33 nm
e
Polarized FT-IR spectra of as-formed [HPC$_{C4}$]^{CF} obtained by SF-ASP after washing
N–H
C–H
C=O
θ = 0°
15°
30°
45°
60°
75°
90°
Absorbance
Wavenumber (cm^{-1})
f
A possible structure of [HPC$_{C4}$]^{CF}
Longer axis of fiber
H-bonding interactions

Fig. 3 | Characterization of $[^{H}PC_{C4}]^{CF}$ obtained by SF-ASP. **a**, POM image of as-formed $[^{H}PC_{C4}]^{CF}$ by SF-ASP, after washing with methanol at 25 °C. White arrows represent transmission axes of the polarizer (P) and analyzer (A). Scale bar, 100 μm. **b**, PXRD pattern of as-formed $[^{H}PC_{C4}]^{CF}$ by SF-ASP, after washing with methanol at 25 °C (Miller indices in parentheses) and schematic illustration of its columnar order with a 2D hexagonal geometry. **c**, Through-view 2D SAXS pattern of a single fiber of $[^{H}PC_{C4}]^{CF}$ (inset; scale bar, 100 μm) obtained by SF-ASP, after washing with methanol at 25 °C (Miller indices are in parentheses). The circle in inset represents the area exposed to an X-ray beam. **d**, SAED pattern of a single fiber of $[^{H}PC_{C4}]^{CF}$ obtained by SF-ASP, after washing with methanol at 25 °C. The *c* axis of the crystalline lattice is parallel to the longer axis of the fiber, while the *ab* plane is perpendicular to it. **e**, Polarized FT-IR spectra at different azimuthal angles (θ) from 0° to 90° of a single fiber of $[^{H}PC_{C4}]^{CF}$ (inset; scale bar, 100 μm) obtained by SF-ASP, after washing with methanol at 25 °C. θ is defined as 0° when the polarizing direction of incident light (P) is parallel to the *c* axis of the crystal. **f**, Wireframe representation of a possible structure of $[^{H}PC_{C4}]^{CF}$, where hydrogen atoms and side chains are omitted for clarity. Red broken lines denote the H-bonding interaction of the amide units.

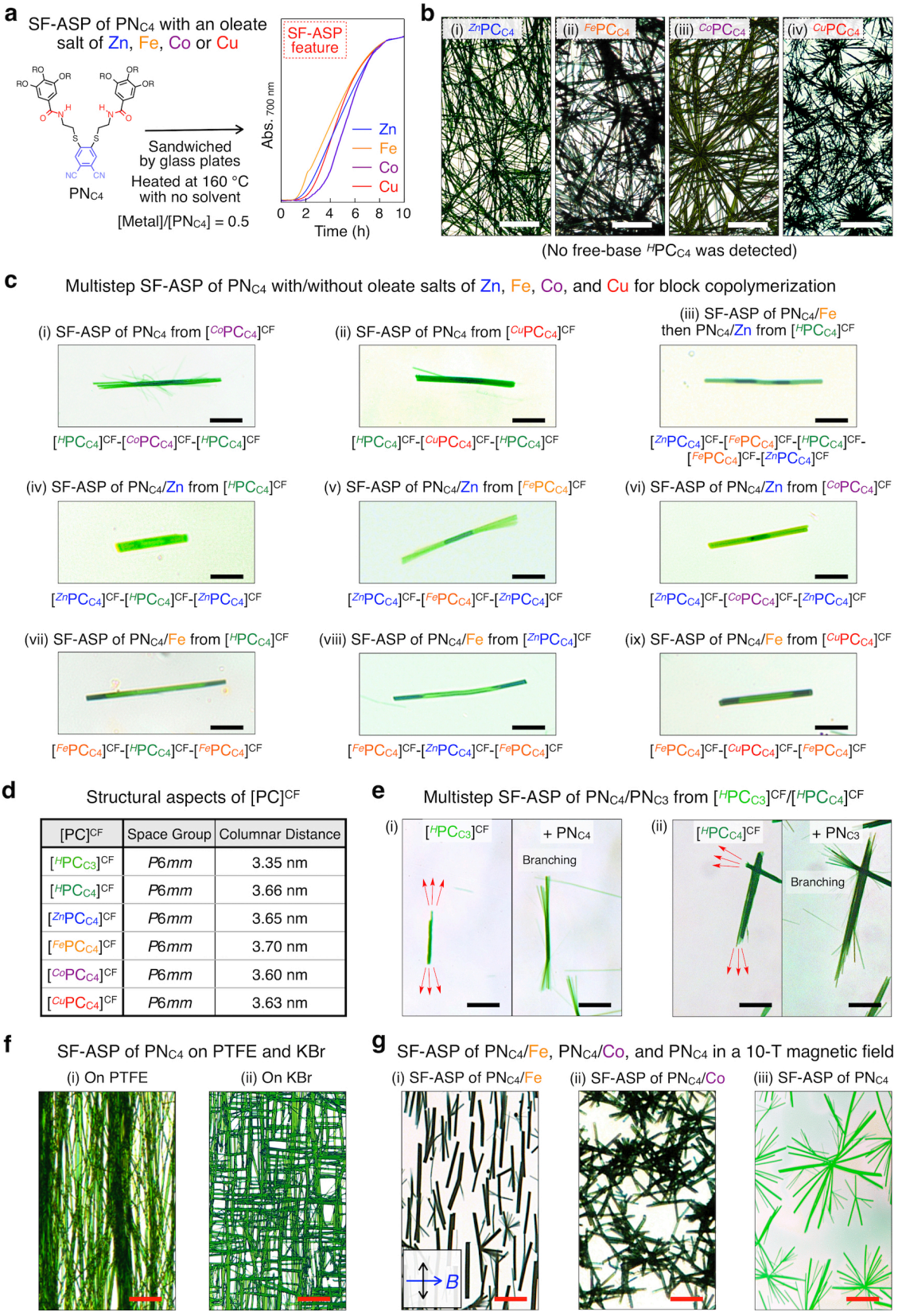

Fig. 4 | Sequence and orientation controls of single-crystalline fibers obtained by SF-ASP. **a**, Time-dependent absorption spectral changes at 700 nm of the reaction mixtures

obtained by the SF-ASP of PN_{C4} in the presence of the oleate salts of Zn (blue), Fe (orange), Co (purple), and Cu (red) (2:1 mole ratio), sandwiched with glass plates upon heating at 160 °C. **b**, Optical images of the reaction mixtures obtained by the SF-ASP of PN_{C4} with the oleate salts of Zn (i), Fe (ii), Co (iii), and Cu (iv) upon heating at 160 °C for 12 hours. Scale bars, 100 μm. **c**, Optical images of the reaction mixtures obtained upon heating at 180 °C for 2–4 hours by the sequential multistep SF-ASP of PN_{C4} with/without the oleate salts of Zn, Fe, Co, and Cu, sandwiched with glass plates covered by CYTOP™ thin films. Scale bars, 30 μm. **d**, Structural parameters of the single-crystalline fibers based on PXRD data. **e**, Optical images showing the changes of the $[^{H}PC_{C3}]^{CF}$ seeds in a hot melt of PN_{C4} (i) and the $[^{H}PC_{C4}]^{CF}$ seeds in a hot melt of PN_{C3} (ii) at 180 °C for 4 hours. Scale bars, 50 μm. **f**, Optical images of the reaction mixtures obtained by the SF-ASP of PN_{C4} with 1-dodecanethiol (0.5 equiv.), sandwiched with two parallelly oriented PTFE-rubbed glass plates (i) and single-crystalline KBr plates (ii) after heating at 180 °C for 12 hours. Scale bars, 50 μm. **g**, Optical images of the reaction mixtures obtained by the SF-ASP of PN_{C4} with $Fe(oleate)_3$ (i) or $Co(oleate)_2$ (ii) and without metal oleates (iii) in a 10-*T* magnetic field after heating at 160 °C for 6 hours. Scale bars, 50 μm. Black and blue arrows represent the directions of $[^{Fe}PC_{C4}]^{CF}$ and the magnetic flux line applied, respectively.

Methods

Materials. Unless otherwise noted, the reagents were used as received from Tokyo Chemical Industry [*N*-hydroxysuccinimide (NHS), sodium hydride (NaH), iodomethane (MeI), 1,8-diazabicyclo[5.4.0]undec-7-ene (DBU), 1-dodecanethiol (DCTH)] and Wako Pure Chemical Industry [*N,N′*-dicyclohexylcarbodiimide (DCC), trifluoroacetic acid (TFA), triethylamine (Et_3N), potassium carbonate (K_2CO_3), zinc(II) acetate, 1-pentanol, and other anhydrous solvents, such as 1,4-dioxane, tetrahydrofuran (THF), dichloromethane (CH_2Cl_2), and chloroform ($CHCl_3$)]. CYTOP™ was purchased from AGC Chemical Company. Single-crystalline potassium bromide (KBr) plates (5.0 mm × 5.0 mm) were purchased from JACSO Int. Co., Ltd. 4,5-Bis(*tert*-butyl ethylcarbamate-2-thio)phthalonitrile[45], 3,4,5-trialkyloxybenzoic acids[46,47], and zinc(II)[48], iron(III)[49], cobalt(II)[50], and copper(II)[51] oleates were prepared according to the reported procedures. Highly oriented glass plates rubbed by a polytetrafluoroethylene (PTFE) rod were fabricated according to a reported method[52]. Dithioalkylphthalonitrile derivatives[45] were synthesized according to the previously reported procedures and unambiguously characterized by ^1H and ^{13}C NMR spectroscopy and matrix-assisted laser desorption ionization time-of-flight (MALDI-TOF) mass spectroscopy. The details of synthetic procedures and characterization data are provided in Supplemental Methods.

General. Column chromatography was carried out with Wako C-300 silica gel (particle size: 45–75 μm). ^1H and ^{13}C NMR spectra were recorded with a JEOL JNM-ECA500 spectrometer operated at 500 and 125 MHz, respectively, where chemical shifts (in ppm) were determined with respect to tetramethylsilane used as an internal reference. MALDI-TOF mass spectrometry was performed with an Applied Biosystems MDS SCIEX 4800 Plus MALDI TOF/TOF™ analyzer using dithranol as the matrix. Infrared (IR) spectra were recorded at 25 °C by a JASCO FT/IR-4100 Fourier transform (FT) IR spectrometer equipped with attenuated total reflection (PRO450-S). Polarized FT-IR spectra were recorded at 25 °C using a JASCO FT/IR-4100 Fourier transform infrared spectrometer connected to an Irtron IRT-5000 microscope unit. UV–vis absorption spectra and time-dependent spectra obtained by a detection at a fixed wavelength were recorded with a JASCO V-670 UV/VIS/NIR spectrophotometer with an FP82HT hot stage. Differential scanning calorimetry (DSC) was performed with a Mettler–Toledo DSC1 star system, where temperature and enthalpy were calibrated with In (430 K, 3.3 J mol^{-1}) and Zn (692.7 K, 12 J mol^{-1}) standard samples using sealed Al pans. Cooling and heating profiles were analyzed using the Mettler–Toledo STAR^e software system. Optical microscopy (OM) and polarizing optical microscopy (POM) were performed with a Nikon Eclipse LV100POL polarizing optical microscope equipped with a Mettler–Toledo FP90 controller attached to an FP82HT

hot stage and a high-definition camera. OM images recorded for the formation of single-crystalline fibers with time were analyzed using ImageJ software. To evaluate the number of generating sites, the positions where single-crystalline fibers began to grow were measured. To evaluate the number and thickness of single-crystalline fibers, all of the as-formed fibers obtained in an OM image were measured and fitted by normal distribution functions. Size-exclusion chromatography (SEC) was performed at 40 °C with a TOSOH HLC-8320GPC system equipped with a refractive index (RI) detector, and $CHCl_3$ was used as an eluent and introduced at a flow rate of 0.35 mL min^{-1} through three linearly connected polystyrene TSKgel SuperHM columns. Powder X-ray diffraction (PXRD) measurements were performed with a Rigaku SmartLab powder X-ray diffractometer equipped with a 3 kW Cu anode (Cu K_α radiation, λ = 1.54 Å). The 2θ angles and the position of the incident X-ray on the detector were calibrated using several reflections obtained from layered silver behenate (d = 58.380 Å). Crystalline fibers were placed in a 1.5 mm-ϕ glass capillary at 25 °C. Small angle X-ray scattering (SAXS) experiments were carried out at BL45XU (X-ray wavelength, λ = 1.08 Å) in Spring-8 (Hyogo, Japan) with an R-AXIS IV++ imaging plate area detector (Rigaku). The sample-to-detector distance used for the SAXS measurements was 1.50 m. Selected area electron diffraction (SAED) collected by transmission electron microscopy (TEM) was performed with an FEI Titan3 TM80-300S/TEM system with an accelerating voltage of 80 kV. Scanning electron microscopy/energy dispersive X-ray (SEM-EDX) spectroscopy were performed using a Hitachi SU8230 field emission scanning electron microscope operated with an accelerating electron beam voltage of 25 kV and equipped with a Bruker X-Flash 6160 EDX detector. A JASTEC JMTD-10T100 superconducting magnet with a vertical bore size of 100 mm was used for the magnetic orientation of crystalline fibers.

Solvent-free synthesis of single-crystalline phthalocyanines and their metal complexes. Typically, a powdery sample (~1 mg) of PN_{C4} was sandwiched with two identical glass plates (25 mm × 25 mm). Upon heating to the isotropic state, a hot melt of PN_{C4} was fully wetted between glass plates and kept at 160 °C for 24 hours. After being cooled to 25 °C, the as-formed $[^{H}PC_{C4}]^{CF}$ were isolated by washing with methanol (10 mL) to remove the unreacted PN_{C4} and side products. By a procedure similar to that for $^{H}PC_{C4}$ except heating at 160 °C for 12 hours under N_2, metallophthalocyanines were obtained from the mixtures of PN_{C4} and metal (Zn, Fe, Co, and Cu) oleates (0.5 equiv.). The as-formed $[^{Zn}PC_{C4}]^{CF}$, $[^{Fe}PC_{C4}]^{CF}$, $[^{Co}PC_{C4}]^{CF}$, and $[^{Cu}PC_{C4}]^{CF}$ were isolated by washing with methanol (10 mL) and hexane (10 mL) to remove the unreacted PN_{C4}, side products, and excessed oleate salts.

Chemical analysis of the reaction mixtures obtained by SF-ASP. A hot melt of PN_{C4} (M mg) was sandwiched with glass plates upon heating at a certain temperature for 24 hours. After 10 minutes of sonication, the reaction mixture was completely dissolved in $CHCl_3$ (1.0

mL), and accordingly, the total concentration of substance was C_M (g L^{-1}). By SEC analysis (Supplementary Fig. 3), the unreacted PN_{C4} and $^{H}PC_{C4}$ in the resulting solution were separated, where the intensity of the signals corresponding to their RI intensity was determined. By calibrating with the concentration-dependent standard curves (Supplementary Fig. 4) of PN_{C4} and $^{H}PC_{C4}$, the concentration fractions of unreacted PN_{C4} and $^{H}PC_{C4}$ were estimated to be C_{PN} (g L^{-1}) and C_{PC} (g L^{-1}), respectively (Supplementary Table 1). Therefore, the weight fractions (%wt.) of the PN_{C4}, $^{H}PC_{C4}$, and others in the reaction mixture were evaluated by the following equations (1) – (3):

$$\%wt._{PN} = (C_{PN}/C_M) \times 100\% \quad (1)$$

$$\%wt._{PC} = (C_{PC}/C_M) \times 100\% \quad (2)$$

$$\%wt._{others} = 100\% - \%wt._{PN} - \%wt._{PC} \quad (3)$$

Sequence control of single-crystalline multi-block fibers obtained by multistep SF-ASP. Typically, active single-crystalline seeds were prepared by chopping the as-formed $[^{H}PC_{C4}]^{CF}$ or $[^{M}PC_{C4}]^{CF}$ for 10 seconds in methanol. The resulting suspension was cast onto a glass plate coated with a transparent thin film of CYTOP™ and air-dried at 25 °C. This glass plate was covered with PN_{C4} premixed with/without metal oleates (0.5 equiv.), and the mixture, which was sandwiched with another glass plate coated by CYTOP™, was heated at 180 °C for 2–4 hours (Supplementary Fig. 14). The single-crystalline fibers were isolated by washing with hexane (10 mL) and methanol (10 mL), affording the ABA-type of triblock fibers. By repeating the above procedure using the ABA-type of triblock fibers as active seeds, the ABCBA-type of multiblock fibers was obtained.

Orientation control of single-crystalline fibers obtained by SF-ASP. Typically, a mixture of PN_{C4} and DCTH (H^+/e^- donor, 0.5 equiv.) was sandwiched with two parallelly oriented glass plates rubbed in advance by a PTFE rod. After heating at 180 °C for 12 hours, the as-formed $[^{H}PC_{C4}]^{CF}$ were obtained and aligned parallel to the rubbed direction of PTFE chains (Fig. 4f, i). By using a procedure similar to the above condition except using the single-crystalline KBr plates as substrates[53], the resulting fibers of $[^{H}PC_{C4}]^{CF}$ were orthogonally grid-like crosslinked (Fig. 4f, ii). According to the method reported for the magnetic orientation[54], a heater with a glass cell of PN_{C4} and its mixtures of $Fe(oleate)_3$ and $Co(oleate)_2$ (0.5 equiv.) was placed in the bore of a superconducting magnet and then kept at 160 °C for 6 hours. The resulting fibers of $[^{Fe}PC_{C4}]^{CF}$ were obtained and aligned

perpendicular to the direction of the applied magnetic flux line (Fig. 4g, i), whereas either $[^{Co}PC_{C4}]^{CF}$ (Fig. 4g, ii) or $[^{H}PC_{C4}]^{CF}$ (Fig. 4g, iii) were randomly oriented under the same conditions.

Data availability

All data that support the findings of this study are available in the main text and the supplementary information and/or from the corresponding authors on reasonable request.

References

45. Miyajima, D. et al. Columnar liquid crystal with spontaneous polarization along the columnar axis. *J. Am. Chem. Soc.* **132**, 8530–8531 (2010).

46. Terazzi, E. et al. Molecular control of macroscopic cubic, columnar, and lamellar organizations in luminescent lanthanide-containing thermotropic liquid crystals. *J. Am. Chem. Soc.* **127**, 888–903 (2005).

47. Achalkumar, A. S. et al. Self-assembly of hekates-tris(n-salicylideneaniline)s into columnar structures: synthesis and characterization. *J. Org. Chem.* **78**, 527–544 (2013).

48. Chiu, W. S. et al. Synthesis of two-dimensional ZnO nanopellets by pyrolysis of zinc oleate. *Chem. Eng. J.* **142**, 337–343 (2008).

49. Bronstein, L. M. et al. Influence of iron oleate complex structure on iron oxide nanoparticle formation. *Chem. Mater.* **19**, 3624–3632 (2007).

50. Buck, M. R., Biacchi, A. J. & Schaak, R. E. Insight into the thermal decomposition of Co(II) oleate for the shape-controlled synthesis of wurtzite-type CoO nanocrystals. *Chem. Mater.* **26**, 1492–1499 (2014).

51. Clary, D. R. & Mills, G. Photochemical generation of nanometer-sized Cu particles in octane. *J. Phys. Chem. C* **115**, 14656–14663 (2011).

52. Wittmann, J. C. & Simth, P. Highly oriented thin films of poly-(tetrafluoroethylene) as a substrate for oriented growth of materials. *Nature* **352**, 414–417 (1991).

53. Yoshimoto, N., Sato, T., Sato, Y. & Ogawa, S. Epitaxial relationships of para-sexiphenyl thin films on alkali halide substrates. *Mol. Cryst. Liq. Cryst.* **425**, 279–288 (2004).

54. Liu, M. et al. An anisotropic hydrogel with electrostatic repulsion between cofacially aligned nanosheets. *Nature* **517**, 68–72 (2015).

Acknowledgements

We appreciate Dr. Cheng Zhang (RIKEN) and Mr. Hao Gong (The University of Tokyo) for generous experimental supports. This work was financially supported by the Japan Society for the Promotion of Science (JSPS) through its Grants-in-Aid for Specially Promoted Research (25000005) on “Physically Perturbed Assembly for Tailoring High-Performance Soft Materials with Controlled Macroscopic Structural Anisotropy” for T.A. D.M. thanks JSPS for a Young Scientist A (15H05487), Coordination Asymmetry (JP17H05394).

Author contributions

Z.C. designed and preformed all experiments. Y.S., A.I., and X.J. designed and assisted partial experiments and analyzed the data. K.V.R., Y.O., E.S., and A.N. performed partial synthetic experiments. D.M. and T.A. conceived the project and co-designed the experiments. Z.C., D.M., and T.A. analyzed the data and wrote the manuscript.

Competing interests

The authors have no competing interests.

Additional information

Supplementary information is available for this paper at http://XXX
Correspondence and requests for materials should be address to T.A. or D.M.
Reprints and permissions information is available at www.nature.com/reprints
Publisher’s note: Springer Nature remains neutral with regard to jurisdictional claims in published maps and institutional affiliations.